# High-resolution simulations of a turbulent boundary layer impacting two obstacles in tandem

Marco Atzori [*]
*Department of Particulate Flow Modelling, Johannes Kepler University, Linz 4040, Austria*

Pablo Torres
*Instituto Universitario de Matemática Pura y Aplicada, Universitat Politècnica de València, Valencia 46022, Spain*

Alvaro Vidal
*Parallel Works, Chicago, Illinois 60654, USA*

Soledad Le Clainche
*School of Aerospace Engineering, Universidad Politècnica de Madrid, Madrid 28040, Spain*

Sergio Hoyas
*Instituto Universitario de Matemática Pura y Aplicada, Universitat Politècnica de València, Valencia 46022, Spain*

Ricardo Vinuesa [†]
*FLOW, Engineering Mechanics, KTH Royal Institute of Technology, Stockholm 10044, Sweden*

(Received 26 April 2022; accepted 16 May 2023; published 15 June 2023; corrected 9 August 2023)

High-fidelity large-eddy simulations of the flow around two rectangular obstacles are carried out at a Reynolds number of 10 000 based on the freestream velocity and the obstacle height. The incoming flow is a developed turbulent boundary layer. Mean-velocity components, turbulence fluctuations, and the terms of the turbulent-kinetic-energy budget are analyzed for three flow regimes: skimming flow, wake interference, and isolated roughness. Three regions are identified where the flow undergoes the most significant changes: the first obstacle's wake, the region in front of the second obstacle, and the region around the second obstacle. In the skimming-flow case, turbulence activity in the cavity between the obstacles is limited and mainly occurs in a small region in front of the second obstacle. In the wake-interference case, there is a strong interaction between the freestream flow that penetrates the cavity and the wake of the first obstacle. This interaction results in more intense turbulent fluctuations between the obstacles. In the isolated-roughness case, the wake of the first obstacle is in good agreement with that of an isolated obstacle. Separation bubbles with strong turbulent fluctuations appear around the second obstacle.

DOI: 10.1103/PhysRevFluids.8.063801

[*] marco.atzori@jku.at
[†] rvinuesa@mech.kth.se

 

## I. INTRODUCTION

Urban areas are a vital element of our society: Currently, about 75% of the population lives in cities in the European Union (EU), and it is estimated that by 2050, seven out of every ten people in the world will become urban residents [1]. Approximately 90% of the urban population in the EU was exposed to air pollution levels that exceeded the levels recommended by the World Health Organization. Pollution leads to around 800 000 premature deaths in Europe every year [2,3]. Moreover, sustainable cities are the 11th sustainable development goal of the United Nations. Therefore, there is an urgent need to improve forecasting and assessment methods to meet these challenges and achieve urban sustainability soon.

For the reasons above, the flow around buildinglike obstacles has been extensively studied [4–6] to improve pollutant dispersion, heat propagation, or energetic efficiency. For a complete review of these methods, we refer the reader to Ref. [7]. These studies are mainly based on empirical observations, meteorologic models, or experimental results. However, turbulence is present in a wide variety of physical phenomena, and urban environments are certainly no exception [8]. In this work we present a numerical study to analyze the interaction of a developed turbulent boundary layer with two buildings in three different configurations.

Overall, the studies dealing with urban flows can be gathered around three main lines of investigation: experimental, numerical, and data driven. Experimental studies tend to combine empirical descriptions of the flow with specific physical quantities measurements that are relevant to analyzing the flow dynamics. These kinds of works are usually divided by their scope. On the one hand, we find studies that characterize the overall dynamics of the flow in urban environments. Within this group, Oke [8] observed that three zones of disturbance could characterize the flow in the envelope of a squared cross-section obstacle: ahead of the obstacle, a bolster eddy vortex, and behind, a lee eddy that is drawn into a cavity of low pressure. Finally, a wake region appears downstream, characterized by increased turbulent intensity but lower horizontal speeds. In this way, fully understanding urban flows inevitably leads to the study of turbulence. We can also mention the work of Britter and Hanna [9], describing the urban environment in terms of the length scale. These authors divided the urban environment into a wide range of scales bounded by the regional (from 10 to 200 km) and neighborhood (from 100 m to 2 km) scales. The present work deals with only the latter.

On the other hand, we find experimental studies that focus on particular flow applications. For instance, Di Sabatino *et al.* [10] carried out the Phoenix urban heat island experiment, in which an extensive database of temperature measurements in various areas of central Phoenix, Arizona, was gathered. The authors used this database to study the urban heat island (UHI) in central Phoenix and validate UHI models. Similarly, Weerasuriya *et al.* [11] assessed the effect of twisted winds on pedestrian comfort. A scaled model of Tsuen Wan Street in Hong Kong was tested in a wind tunnel to obtain the mean flow, turbulent intensities, and yaw angles. Pedestrian comfort was also studied experimentally by Corke *et al.* [12], and pollutant dispersion was assessed in a number of urban environments by Nagib and Corke [13] and Monnier *et al.* [14]. More complicated geometries were also analyzed experimentally by Monnier *et al.* [15].

Numerical simulations, even though they are limited by the computational cost, can provide a detailed description of the flow properties and have been used to characterize the overall dynamics of urban flows. There is a wide range of numerical methods available with different levels of accuracy. Reynolds-averaged Navier-Stokes (RANS) simulations, in which all turbulent scales are modeled, are not able to fully characterize the physical processes that take place in urban environments [16,17], so direct numerical simulations (DNSs) and large-eddy simulations (LESs) are usually employed. The LES category also encompasses a wide range of resolutions, where subgrid models can represent a larger or smaller portion of turbulent scales.

Similarly to experimental studies, numerical ones also differ in the type of geometrical model being considered. The choice of a different balance between geometrical complexity, simulation accuracy, and computational cost led to the creation of a few distinct kinds of study cases. We summarize the most recent papers that are relevant to the context of the present work in Table I.

TABLE I. Summary of studies relevant to the present paper. In cases with multiple simulations, the one at highest Reynolds number is shown. For inflow conditions, $\overline{U}$ + STF denotes prescribed mean flow with synthetic turbulent fluctuations and PS denotes a precursor simulation. We include the number of points per obstacle edge ($n_p$) or the grid spacing in physical ($\Delta_x$) or inner-scaled units ($\Delta_x^+$), as well as the total number of grid points in millions ($N_p/10^6$).

| Reference | Obstacle(s) | Inflow | $\mathrm{Re}_H$ | Methodology | $N_p/10^6$ | Main focus or aim |
|---|---|---|---|---|---|---|
| Kanda *et al.* [18] | array | periodic | $5 \times 10^3$ | LES ($n_p = 10$) | 1.4 | effects of obstacle areal density |
| Xie and Castro [19] | array | periodic | $5 \times 10^6$ | LES ($n_p = 16$) | 0.25 | comparison of DNS, LES, and RANS |
| Tseng *et al.* [20] | array | periodic | $2.2 \times 10^4$ | LES ($n_p \leqslant 10$) | 0.8 | LES validation |
| Coceal *et al.* [21] | array | periodic | $5 \times 10^3$ | LES ($n_p = 32$) | 50 | test theoretical frameworks |
| El-Okda *et al.* [22] | one rectangular | $\overline{U}$ + STF | $30 \times 10^3$ | LES | 1.4 | flow statistics and inflow conditions |
| Bou-Zeid *et al.* [23] | urban model | PS | | LES ($\Delta_x = 15$ m) | 0.8 | surface modeling |
| Santiago *et al.* [24] | array | steady profile | $1 \times 10^6$ | LES ($n_p = 11$) | 1.6 | comparison of LES and RANS |
| Kono *et al.* [25] | array | periodic | $1.3 \times 10^4$ | LES ($n_p = 32$) | 10.6 | aid modeling |
| Einian *et al.* [26] | one rectangular | steady profile | 500 | LES ($n_p \simeq 6$) | 1.8 | subgrid model effects |
| Nakayama *et al.* [27,28] | urban model | $\overline{U}$ + STF | | LES ($\Delta_x = 20$ m) | 2.9 | reproduce atmospheric phenomena |
| Saha [29] | one rectangular | uniform | 250 | DNS ($n_p = 34$) | 1.8 | vortex shedding, separation, and drag |
| Saeedi *et al.* [30] | one rectangular | $\overline{U}$ + STF | $1.2 \times 10^4$ | DNS ($\Delta_x^+ = 0.8$) | 35 | mean, fluctuations, and TKE budget |
| Jourbet *et al.* [31] | one rectangular | $\overline{U}$ + STF | $7.6 \times 10^4$ | LES ($n_p = 32$) | 3.5 | mean and flow structures |
| Cheng and Porté-Agel [32] | array | PS | $3 \times 10^4$ | LES ($n_p = 10$) | 8 | rural-to-urban transition |
| Vinuesa *et al.* [33] | one rectangular | PS | $1.1 \times 10^4$ | DNS | 250 | inflow effects and flow statistics |
| Giometto *et al.* [34] | urban model | periodic | | LES ($n_p = 30$) | 42 | complement experimental measurements |
| Zhang *et al.* [35] | one rectangular | uniform | $1 \times 10^3$ | DNS ($n_p = 48$) | 14 | flow statistics and vortex shedding |
| Diaz-Daniel *et al.* [36] | one rectangular | PS | $3 \times 10^3$ | DNS ($n_p = 320$) | 538 | interaction between wake laminar and turbulent boundary layers |
| Tolias *et al.* [37] | urban model | $\overline{U}$ + STF | | LES ($\Delta_x = 1.2$ m) | 28 | LES validation |
| Kumar and Tiwari [38] | one rectangular | shear layer | 250 | DNS ($n_p = 140$) | 1.6 | flow structures and transition |
| Tian *et al.* [39] | array | periodic | $5 \times 10^4$ | LES ($n_p = 128$) | 28 | mean, fluctuations, TKE budget, and spectra |
| Zhao *et al.* [40] | two rectangular | uniform | 500 | DNS ($n_p = 60$) | 7.8 | wake interactions and flow statistics |
| present study | two rectangular | ZPG TBL | $1 \times 10^4$ | LES ($n_p = 196$) | 142 | wake interactions and flow statistics |

The first works focused on so-called urban canyons, where the simulation describes the cavity between two rectangular bodies and the laminar freestream flow above [41–43]. Later on, it became possible to consider arrays of obstacles with different arrangements in pattern and packing ration, but still periodic boundary conditions in the direction of the incoming flows, e.g., in Refs. [18,19,21,44]. These types of flow configurations, however, do not allow us to examine the effects of an incoming boundary layer or of the more complex geometries typical of realistic landscapes. We then observed developments in two complementary directions of investigation.

Models for urban geometries have been considered, although they often require one to employ a very low number of grid points per each single obstacle to be affordable. Some of the studies that adopted this perspective have focused on measuring the impact of, e.g., resolution [20], surface modeling [23], and boundary conditions [37] on quantities that can be measured experimentally to assess the reliability of simulations. Others aimed at reproducing specific atmospheric phenomena [27,28] or they provide information not easily measurable in experiments, such as terms of the turbulent-kinetic-energy (TKE) budget [34]. This type of study takes advantage of the fact that the main features of urban flows have a weak dependence on the Reynolds number and therefore can be captured even when a small portion of the active scales are simulated.

On the other hand, simplified geometries have been considered in highly resolved numerical simulations. In certain cases, these studies are aimed at developing or testing models [26], sometimes with the aid of experiments [22,24,31]. In other studies, the main purpose of the authors is to describe the connection between the obstacle geometry and global features of the flow, such as drag coefficients or vortex-shedding frequencies [29,35], or turbulence properties, such as velocity fluctuations, TKE budget, and spectra [30,36,39]. Note that in these studies, an incoming turbulent flow is often implemented as a prescribed mean-velocity profile with synthetic turbulent fluctuations [30,31] or using a precursor simulation [33,36]. The incoming flow in the works just mentioned is not representative of atmospheric conditions.

Only a few of the works employing wall-resolved simulations considered both a combination of obstacles and a developed turbulent flow. For instance, Zhao *et al.* [40] studied the flow between two buildinglike obstacles in several configurations with DNS, with a uniform inlet profile, and at a relatively low Reynolds number of 500 (defined in terms of the obstacle height, the fluid kinematic viscosity, and the incoming velocity). The aim of the present work stems from the lack of high-fidelity numerical simulations for the case of obstacles in tandem subjected to an incoming turbulent boundary layer. For this geometry, as observed at transitional Reynolds numbers [40], the rate between wake length and obstacle distance enables identifying different flow regimes, similarly to what was observed by Oke [8] in urban canyons. We carried out wall-resolved LES, using a resolution that is only a factor of 2 coarser than that of a DNS and a domain size that allows establishing a turbulent boundary layer before the obstacles. Through these simulations we will describe how the flow regimes differ in the distributions of turbulent fluctuations, TKE budgets, and properties of the anisotropy tensor. The conditions that we choose do not correspond to a realistic urban flow yet, but are a step forward with respect to previous works on wall-mounted rectangular obstacles towards fully resolved simulations of a similar system with a larger scale.

The paper is organized as follows. In Sec. II we introduce the computational method and setup used during the simulations. The results of the simulations are presented and discussed in Sec. III. We provide a summary and some closing notes on other lines of investigation on urban flows, including coherent structures, in Sec. IV.

## II. COMPUTATIONAL METHOD AND SETUP

The flow of air in urban environments is characterized by relatively low velocities, well below the speed of sound. Thus, the incompressible Navier-Stokes equations can be used to model the flow. These equations have been solved using the computational-fluid-dynamics code Nek5000, which was developed by Fischer *et al.* [45]. Nek5000 is based on the spectral-element method (SEM) developed by Patera [46], which combines the geometrical flexibility of the finite-element

method with the accuracy of the global spectral methods. Within the elements, the governing equations are discretized using a Galerkin projection in the so-called $\mathbb{P}_N-\mathbb{P}_{N-2}$ formulation. In this formulation, $\mathbb{P}_N$ denotes the polynomial space of the trial function for the velocity, where $N$ is the maximum order, and $\mathbb{P}_{N-2}$ denotes the space of the trial functions for the pressure. The space of the trial function for the pressure reaches a maximum order of $N-2$, because the pressure is defined on a staggered grid within each element without points on the element edges. Nek5000 has been extensively used for turbulent-flow simulations in complex geometries [47–51], and it is thus adequate for the urban-environment cases considered here. The turbulence statistics are computed with the toolbox developed by Vinuesa *et al.* [52].

The complexity of turbulent urban flows requires using high-fidelity methods to resolve the relevant flow structures correctly. Direct numerical simulations are often used in wall-bounded turbulent flows [53,54]; however, in the case of urban environments, the presence of obstacles forbids the use of classical tools of DNS such as fast Fourier methods [55,56], making computational cost unaffordable. In the present work we conduct wall-resolved LES, the resolution criterion of which is close to that of a coarse DNS. The LES filter is based on the approximated deconvolution model proposed by Schlatter *et al.* [57]. The implementation and validation of this filter in Nek5000 are extensively documented by Negi *et al.* [58], who obtained excellent agreement with DNS statistics in turbulent wings while significantly reducing the computational cost. The same methodology has also been recently examined by Rezaeiravesh *et al.* [59], who used various uncertainty-quantification techniques to describe how grid spacing and filter parameters affect the solution. In these simulations, the governing equations for the filtered velocity are written in dimensionless form as

$$\frac{\partial \tilde{U}_i}{\partial t} + \tilde{U}_j \frac{\partial \tilde{U}_i}{\partial x_j} = -\frac{\partial P}{\partial x_i} + \frac{1}{Re_h}\frac{\partial^2 \tilde{U}_i}{\partial x_j \partial x_j} - \mathcal{H}(\tilde{U}_i), \tag{1}$$

$$\frac{\partial \tilde{U}_i}{\partial x_i} = 0\,. \tag{2}$$

The symbol $\mathcal{H}(\tilde{U}_i)$ denotes the LES relaxation that acts as a volume force, and dealiasing with overintegration is used to evaluate the nonlinear term of the momentum equation. The effect of the filter is to remove energy from the system by acting on a subset of modes within each spectral element. Hereafter, we drop the symbol of filtered quantities for the sake of brevity. The operator $\mathcal{H}$ is written as a high-pass filter in the frequency domain, i.e.,

$$H(u_N) = \chi \sum_{k=0}^{N} \gamma_k a_k L_k, \tag{3}$$

where $L_k$ and $a_k$ denote the Legendre polynomials and spectral coefficients, respectively, $N$ is the polynomial order, $\chi$ is the filter weight, and $\gamma_k$ is the filter transfer function, which is defined as

$$\gamma_k = \begin{cases} 0, & k \leqslant k_c \\ \left(\frac{k-k_c}{N-k_c}\right)^2, & k > k_c, \end{cases} \tag{4}$$

where $k_c$ is the cutoff mode. The cutoff mode, which is the same for all elements, the polynomial order, and the size of each spectral element determine the local cutoff frequency within elements. The filter with this definition does not affect continuity and its intensity does not depend on the time interval.

The instantaneous velocity field is denoted by $\boldsymbol{U}(x, y, z, t)$, where $x$, $y$, and $z$ are the streamwise, vertical, and spanwise directions, respectively, and $t$ is time (a visualization of the solution at an arbitrary time step is provided in Fig. 1). The pressure is denoted by $P$. The three components of the velocity in the spatial directions are $\boldsymbol{U} = (U, V, W)$. Note that the indices $i$ and $j$ run from 1 to 3, spanning through the spatial coordinates, and that Einstein's

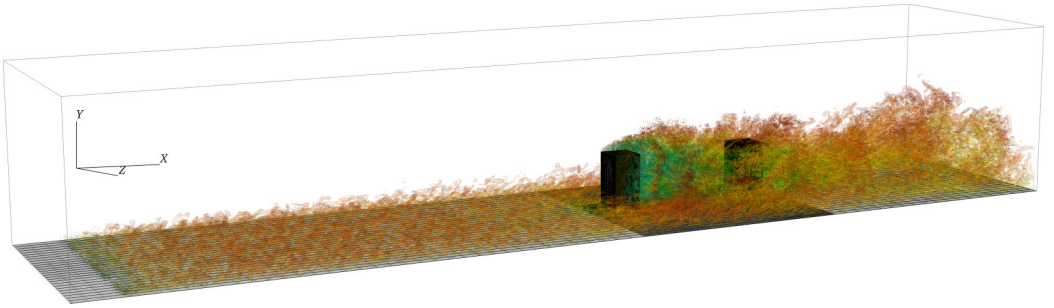


FIG. 1. Overview of the computational domain for the wake-interference case with vortex clusters identified with the $\lambda_2$ criterion [60] (we show the isosurface $\lambda_2 = -1$) and colored with the streamwise velocity component (values from approximately $-1$ in blue to approximately 2 in red).

notation of summation for repeated indices is applied. All length quantities are normalized using the obstacle height, denoted by $h$, and the velocity scale is the freestream value, denoted by $U_\infty$. The Reynolds number $\mathrm{Re}_h = U_\infty h/\nu$ is based on the freestream velocity, the obstacle height, and the kinematic viscosity. Following the Reynolds decomposition, $\boldsymbol{U}$ is defined as $\boldsymbol{U} = \overline{\boldsymbol{U}} + \boldsymbol{u}$, where $\overline{\boldsymbol{U}}$ is the average in time and $\boldsymbol{u}$ is the turbulent fluctuation. The components of the Reynolds-stress tensor are thus denoted by $\overline{u_i u_j}$.

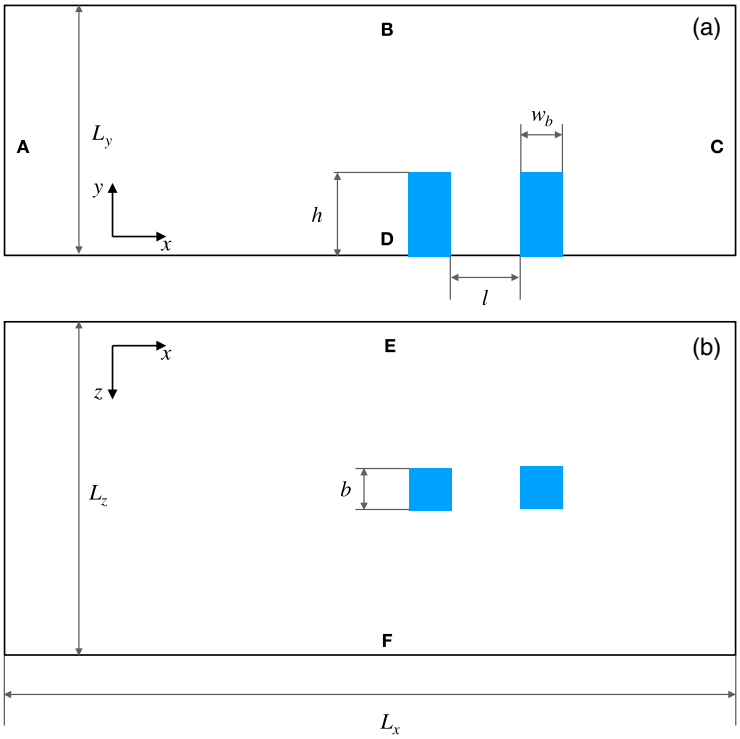


FIG. 2. Schematic representation of the simulation domain from the (a) side and (b) top views. The flow goes from left to right and the obstacles are marked in blue. The center of the first obstacle is at distance of $10h$ from the inflow, and faces A, B, C, D, E, and F are the boundaries of the domain.

TABLE II. Geometrical parameters of the three flow cases under study. The reported number of grid points is based on polynomial order $N = 7$, and the reported averaging periods to obtain turbulence statistics follow 40 convective time units, which are discarded to avoid initial transients. All the averaging periods correspond to over 13 eddy-turnover times, based on the $u_\tau$ and $h$ values of the TBL at $x/h = -2$.

| Case name | Case code | $L_x/h$ | $L_y/h$ | $L_z/h$ | $b/h$ | $w_b/h$ | $l/h$ | No. of grid points | Average period |
|---|---|---|---|---|---|---|---|---|---|
| skimming flow | SF | 16 | 3 | 4 | 0.5 | 0.5 | 1 | $103 \times 10^6$ | 104 |
| wake interference | WI | 17 | 3 | 4 | 0.5 | 0.5 | 2 | $116 \times 10^6$ | 104 |
| isolated roughness | IR | 21 | 3 | 4 | 0.5 | 0.5 | 4 | $142 \times 10^6$ | 105 |

In Fig. 2 we show a schematic representation of the geometry used in the three simulations, where $L_x$, $L_y$, and $L_z$ represent the dimensions of the computational domain in the streamwise, vertical, and spanwise directions, respectively. The vertical and spanwise dimensions are the same in the three cases, while the streamwise dimension of the domain is varied proportionally to the distance between the obstacles $l$. The obstacles are defined using three parameters: $h$, $w_b$, and $b$, their height, length, and width, respectively. Table II gathers the geometrical data of the three cases considered in the present work. In all cases, the Reynolds number is defined with a value of $\mathrm{Re}_h = 10\,000$.

As stated in the Introduction, we present here the results of three different configurations, representative of the three flow regimes documented by Oke [8]. As explained by Sini *et al.* [41], these configurations depend on the ratio $l/h$ as follows: If this ratio is small enough, i.e., for narrow streets, the flow above the buildings only sometimes enters into the space between obstacles, in a configuration denoted by skimming flow (SF). The second situation, wake interference (WI), is present for wider streets, where the wake of the first building interacts with the second one. Finally, the third configuration is called isolated roughness (IR) and it corresponds to very broad streets, where the interaction of the wake of the first building with the second one is small. Table II summarizes the geometrical parameters of the three cases.

The inflow is set at face A (Fig. 2) and the outflow is set at face C. To improve our results, we apply the stabilized outflow developed by Dong *et al.* [61]. In the spanwise direction, i.e., faces E and F, we impose periodicity. At face B we prescribe a stress-free condition in the $y$ direction, zero velocity in the $z$ direction, and we set $U_\infty$ in the $x$ direction. Face D and the faces that form the obstacle are set as solid walls, i.e., no-slip and no-penetration conditions.

### A. Turbulent-boundary-layer development

As discussed in the Introduction, urban flows are turbulent [8]. Thus, we set up the flow so that the incoming turbulent boundary layer (TBL) can develop before reaching the obstacles. In this study the inflow condition is a Blasius laminar profile with $\mathrm{Re}_{\delta^*} = 450$, which is the Reynolds number based on displacement thickness $\delta^*$. Then we trigger the transition to turbulence by employing a numerical tripping force, acting along a horizontal line on the ground wall and at $x = -9h$. Numerical tripping is a technique that consists of introducing a weak random volume in the forcing terms of the incompressible Navier-Stokes equation acting in the wall-normal direction such that disturbances are created in the flow, as documented in Refs. [62,63]. Next we will discuss the turbulence statistics of the TBL upstream of the first obstacle in the SF case, noting that these results are the same in the other two cases.

In Fig. 3(a) we present the streamwise evolution of the friction Reynolds number $\mathrm{Re}_\tau = u_\tau h/\nu$ and the Reynolds number based on momentum thickness $\mathrm{Re}_\theta = U_\infty \theta/\nu$. Here $u_\tau = \sqrt{\tau_w/\rho}$ is the friction velocity, $\tau_w$ is the wall-shear stress, $\rho$ is the fluid density, $\nu$ is the fluid kinematic viscosity, and $\theta$ is the momentum thickness. As expected, $\mathrm{Re}_\theta$ increases with the streamwise coordinate, starting at the application of the tripping force. Upstream of the first obstacle we obtain $\mathrm{Re}_\tau \simeq 175$, which corresponds to fully turbulent conditions. Note that the recirculation region upstream of the first obstacle induces an adverse pressure gradient (APG) on the TBL, which can be characterized

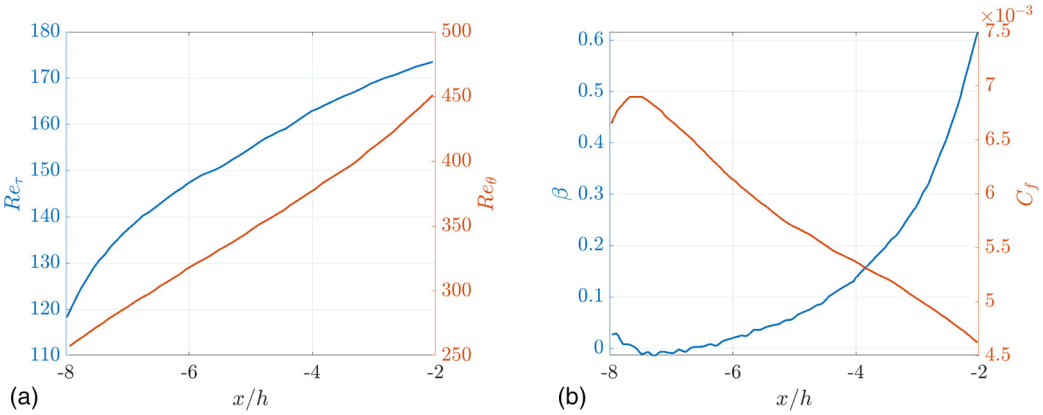


FIG. 3. Streamwise evolution of (a) the friction and momentum-thickness-based Reynolds numbers and (b) the Rota-Clause parameter and the skin-friction coefficient in the region upstream of the first obstacle.

in terms of the Rota-Clauser pressure-gradient parameter $\beta = \delta^*/\tau_w dP_e/dx$, where $dP_e/dx$ is the streamwise pressure gradient at the boundary-layer edge. This parameter and the skin-friction coefficient $C_f = 2(u_\tau/U_e)^2$ (where $U_e$ is the local edge velocity) are shown in Fig. 3(b). Note that the boundary-layer thickness is obtained using the method proposed by Vinuesa *et al.* [64]. The streamwise APG produces the increase of $\beta$ with $x$, reaching a value of around 0.6 at $x/h = -2$. This value corresponds to a moderate APG. The skin-friction coefficient slightly grows between $x/h = -8$ and $-7$, which is explained by the effects of the tripping force. However, $C_f$ decreases in the region upstream of the first obstacle, a behavior consistent with the TBL development and the APG.

The statistics presented in Fig. 3 are validated by the results by Eitel-Amor *et al.* [65] for a zero-pressure-gradient (ZPG) TBL, simulated by wall-resolved LES up to $\mathrm{Re}_\theta = 8300$. In Figs. 4(a) and 4(b) we show the inner-scaled mean-velocity and streamwise-velocity fluctuation profiles of our TBL at various streamwise positions, together with the profiles extracted from Ref. [65]

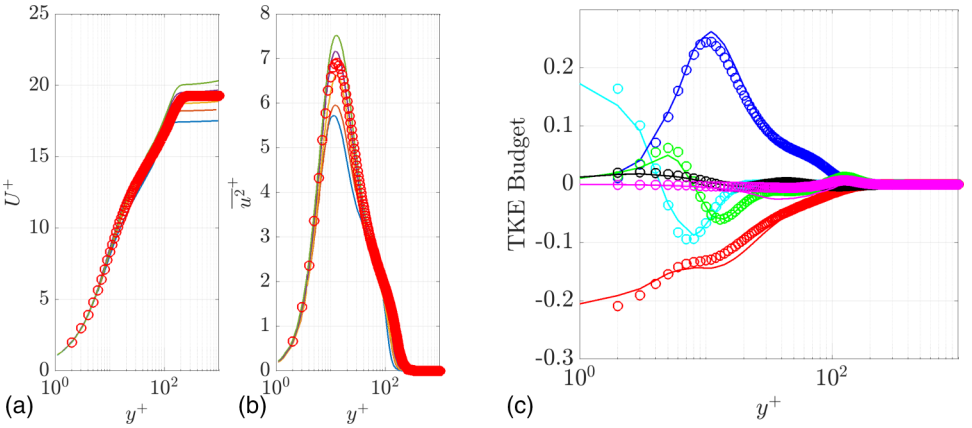


FIG. 4. (a) Inner-scaled mean and (b) velocity-fluctuation profiles at the following streamwise locations: $x/h = -7$ (blue), $x/h = -6$ (red), $x/h = -5$ (yellow), $x/h = -4$ (purple), and $x/h = -3$ (green). The circles represent the profiles from the wall-resolved LES data set by Eitel-Amor *et al.* [65] at the same $\mathrm{Re}_\tau$ as the profile at $x/h = -4$. (c) TKE budget terms at $x/h = -4$, where lines denote data from our simulation and circles results in Ref. [65] at matched $\mathrm{Re}_\tau$. Blue, red, green, cyan, black, and magenta represent production, dissipation, turbulent transport, viscous diffusion, velocity-pressure correlation, and advection terms, respectively.

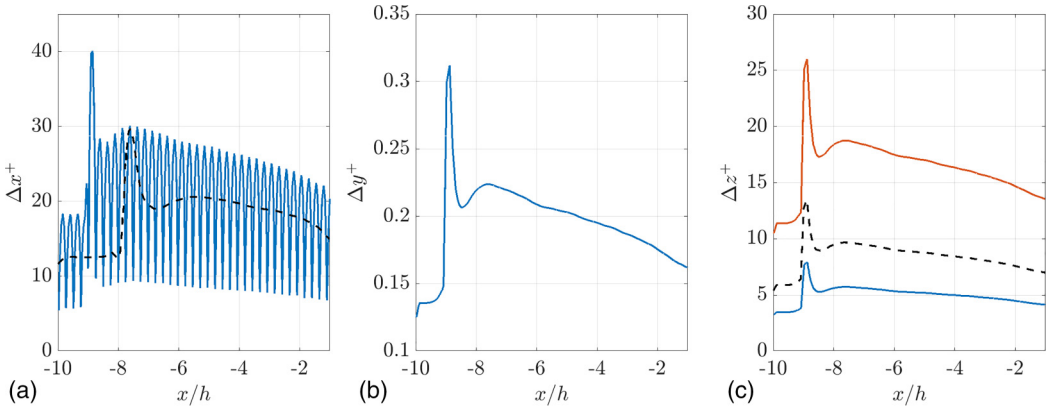


FIG. 5. (a) Streamwise evolution of the inner-scaled resolution in the streamwise direction, where blue denotes the local spacing and the black dashed line the average over the element. (b) Wall-normal resolution of the first grid point. (c) Spanwise resolution, where blue and orange denote the minimum and maximum grid spacings of the element, respectively, and the black dashed line again the average over the element.

at $\mathrm{Re}_\tau \simeq 145$, which is the $\mathrm{Re}_\tau$ of our TBL at $x/h = -4$. Note that we choose this location for comparison because here turbulence has already developed and $\beta \simeq 0.1$, i.e., the TBL is in nearly-ZPG conditions. The various streamwise profiles reflect an adequate TBL development, and comparison at $x/h = -4$ with the ZPG TBL in Ref. [65] shows excellent agreement, a fact that indicates that the incoming TBL is properly simulated. Furthermore, in Fig. 4(c) we compare the terms of the TKE budget in the incoming TBL with those of the same reference [65]. Additional information on the calculation of all the terms can be found in the work by Vinuesa *et al.* [52]. Interestingly, this figure shows that all the terms are in perfect agreement, including the near-wall production peak and the turbulent transport. For $y^+ < 3$, both the TKE dissipation and the viscous diffusion are slightly lower than the reference values, which can be attributed to the small effect of the filter in the smallest scales. Overall, the agreement is entirely satisfactory, a fact that highlights the quality of the present simulations.

### B. Mesh design and resolution

As discussed above, Nek5000 is based on the SEM developed by Patera [46]. The mesh comprises a number of spectral elements, ranging from 200 000 to 280 000 for the cases under consideration here, and each element has a total of $8^3$ points which follow the Gauss-Lobatto-Legendre quadrature. The element size is refined near the wall and the obstacles in order to increase resolution. The mesh is designed following the criteria by Negi *et al.* [58] for wall-resolved LES: In the TBL part, $\Delta x^+ < 18$ and $\Delta z^+ < 9$, which are the inner-scaled resolutions in the streamwise and spanwise directions, respectively, averaged over the spectral elements. Furthermore, $\Delta y^+ < 0.5$, which is the wall-normal resolution of the first grid point in inner units. In Fig. 5 we show the streamwise evolution of these quantities for $x/h < -1$, i.e., for the region upstream of the first obstacle, and it can be observed that the criterion for wall-resolved LES is satisfied within the incoming TBL. Note that the resolution in the $x$ and $z$ directions corresponds to approximately half of that required for a DNS [54]. It is interesting to note that the increase in the streamwise grid spacing at $x/h = -9$ is explained by the tripping force applied at this location. Farther from the wall, an additional requirement is satisfied for mesh resolution: Defining $h = (\Delta x \Delta y \Delta z)^{1/3}$, the ratio $h/\eta < 9$ everywhere in the domain, where $\eta = (\nu^3/\varepsilon)^{1/4}$ is the Kolmogorov scale and $\varepsilon$ is the local isotropic dissipation.

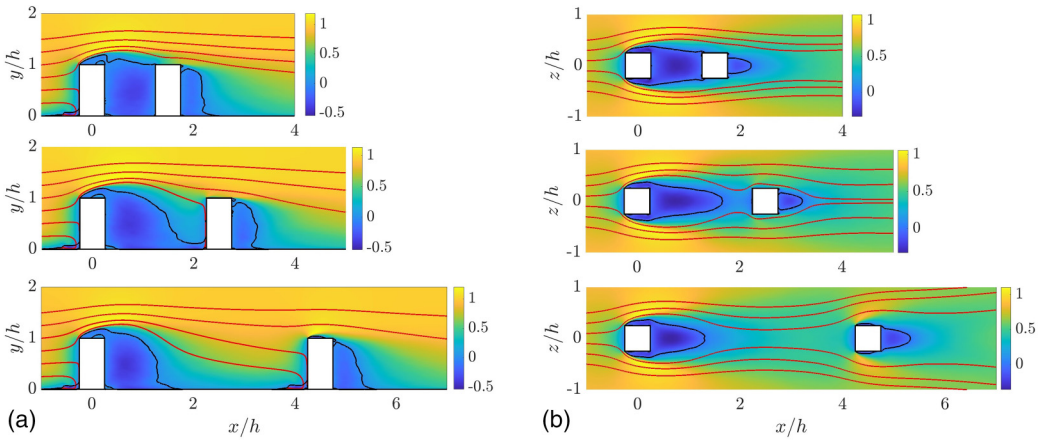


FIG. 6. Mean streamwise velocity $\overline{U}$ at (a) $z/h = 0$ and (b) $y/h = 0.25$. The red lines and black contours denote streamlines and $\overline{U} = 0$, respectively. The streamlines are computed using $\overline{U}$ and $\overline{V}$ for vertical planes and $\overline{U}$ and $\overline{W}$ for horizontal planes (note that streamlines of the 3D mean flow do not lie on the horizontal plane). Shown from top to bottom are the SF, WI, and IR cases.

## III. RESULTS AND DISCUSSION

In this section we analyze the turbulence statistics, including mean velocities, Reynolds stresses, and TKE budgets in a selected portion of the computational domain. We show the statistics at the planes $y/h = 0.25$ and $z/h = 0$. We take advantage of the central symmetry of the case, averaging between the right and left portions of the domain for the statistics on the horizontal plane, $y/h = 0.25$. Note that the following results are presented in outer scaling, i.e., in terms of $U_\infty$ and $h$.

### A. Mean flow

In this section we focus on the properties of the mean flow. The most evident effect of the increasing distance between the obstacles is the transition from a cavitylike flow to a wakelike flow in the region between the two obstacle, as already described by Zhao *et al.* [40] for a slightly different geometry and lower Reynolds number. The cavitylike flow is characterized by a very large circulation zone attached to the rear face of the first obstacle, which transports fluid in a clockwise motion. This feature of the mean flow occupies most of the space between the obstacles. The wakelike flow also exhibits a clockwise circulation zone, but this is limited to the first portion of the space between the obstacles. The second portion of this space, in front of the second obstacle, is occupied by flow that is still moving in the direction of the freestream.

Figure 6 shows the streamwise mean velocity on the planes $z/h = 0$ and $y/h = 0.25$, together with streamlines computed using the mean-velocity components on the two planes. In the SF case, there is only a little penetration of the flow from above the canopy into the cavity. As the distance between the obstacles increases, the wake of the first obstacle becomes more apparent and there are stronger interactions between freestream and cavity regions, as observed in the WI case. For an even higher distances between obstacles, in the IR case, the effects of the second obstacle on the wake of the first are negligible. Interestingly, the wake behind the second obstacle is relatively similar between the three regime, even thought the low speed of the incoming flow avoids the occurrence of separation at the edges in the SF and WI cases.

In Fig. 7 we show the vertical and spanwise mean-velocity components for the three cases. Both of these velocity components are less intense than the streamwise component in most of the domain, with a few notable exceptions. The first exception is the wake regions and the cavity between the obstacle in the SF case, where $\overline{U}$ changes sign. The second one is the separation regions caused by

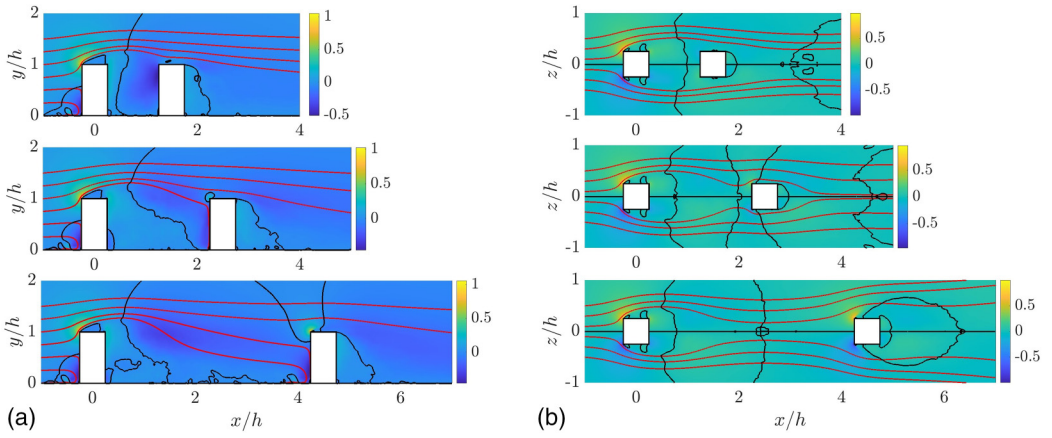


FIG. 7. (a) Mean vertical velocity $\overline{V}$ at $z/h = 0$ and (b) spanwise velocity $\overline{W}$ at $y/h = 0.25$. The red lines and black contours denote streamlines and $V = 0$, respectively. The streamlines are computed using $\overline{U}$ and $\overline{V}$ for vertical planes and $\overline{U}$ and $\overline{W}$ for horizontal planes (note that streamlines of the 3D mean flow do not lie on the horizontal plane). Shown from top to bottom are the SF, WI, and IR cases.

the obstacle edges. These are particularly evident for the first obstacle in all three cases and are also present in the second obstacle in the IR case. The third occurrence of where $\overline{U}$ is not the dominant mean-velocity component is in regions just in front of the obstacles where the flow is deflected downward. This is even more evident for the second obstacle than for the first one, in all cases. The effects of varying intensities and signs of the three velocity components are well summarized in the streamlines computed on the mean flow. In the WI case, where $\overline{U}$ remains high above and around the relatively short cavity, most streamlines with origin before the first obstacle pass over or to the sides of the cavity. The longer cavities in the SF and IR cases however correspond to a longer region of deceleration before the second obstacle. In this region, where $\overline{V}$ is negative, streamlines lying on the vertical plane are deflected downward.

The three flow regimes also differ in how the signs of $\overline{V}$ and $\overline{W}$ change in the domain, which is particularly affected by the change of regime between the SF and WI cases. In the SF case, with the large zone of clockwise mean motion, $\overline{V}$ is negative in most of the region between the obstacles, resembling the pattern of the classical two-dimensional lid-driven cavity. In the WI and IR cases, the region with positive $\overline{V}$ behind the first obstacle expands. In these cases the mean flow is still moving downstream in the higher portion of the wake, but upstream in the lower one. The topology of the mean spanwise velocity $\overline{W}$ at intermediate heights, such as $y/h = 0.25$, is particularly interesting. In front of the first obstacles, the flow is deflected sideways, around the front edges, and it also moves from the center plane towards the outside of the cavity in the wake. In the SF case, $\overline{W}$ changes sign only once, so the flow moves toward the center of the domain in the region in front of the second obstacle. In the WI and IR cases however, at this $y/h$, $\overline{W}$ changes sign at least twice, so the flow in the cavity moves outward behind the first obstacle, inward afterward, and outward again before the second obstacle. These differences in the topology of $\overline{W}$ are yet another aspect of the modification of the mean flow between the SF case, where the second object is completely engulfed by the wake of the first one, and the WI and IR cases, where the wake of the first object is confined between the obstacles. In the IR case, $\overline{W}$ also shows the further development of the wake flow around the second obstacle, due to the appearance of mean separation over the side faces.

There are both similarities and differences between our results and those reported by Zhao *et al.* [40], who also studied the flow around two obstacles but with a lower width-to-height ratio of $w_b/h = 0.25$, with laminar incoming flow, and at $\mathrm{Re}_h = 500$. They considered distances between obstacles up to $l/h = 2$, corresponding to the first two regimes that we examined. The transition between a cavitylike flow in the SF regime and a wakelike flow in the WI regime is also observed,

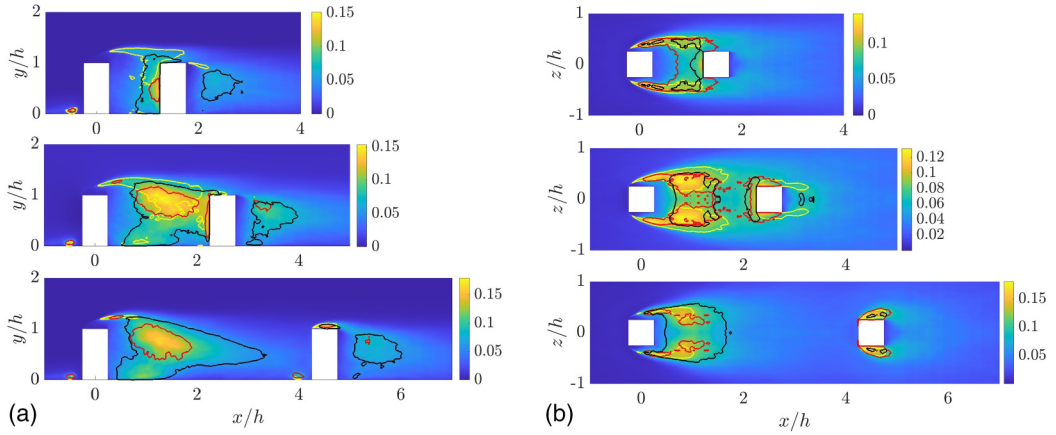


FIG. 8. Turbulent kinetic energy, denoted by $k$, at (a) $z/h = 0$ and (b) $y/h = 0.25$. The yellow, red, and black contours denote regions of high $\overline{u^2}$, $\overline{v^2}$, and $\overline{w^2}$, respectively. In these regions, the considered quantity is higher than $1/3$ of its maximum in the domain. Shown from top to bottom are the SF, WI, and IR cases.

but it already occurs for $l/h = 1.25$, which is a distance lower than that of the SF case in our data set ($l/h = 1.5$). The wake behind the second obstacle seems longer for SF configurations than for WI configurations in the database studied in Ref. [40], a phenomenon that is not as evident in our data. This sort of comparison is however made difficult by the fact that both $\mathrm{Re}_h$ and $w_b/h$ are different between the two studies.

### B. Reynolds stresses

The Reynolds stresses show the distribution of turbulence fluctuations within the domain. In Fig. 8 we illustrate the turbulent kinetic energy, defined as $k = 1/2(\overline{u^2} + \overline{v^2} + \overline{w^2})$, as well as contours highlighting regions of higher values for each of the three components of the Reynolds stress. Turbulence fluctuations tend to be more intense between the two obstacles in all the cases and the horseshoe vortex in front of the obstacles (when present). The highest values of $k$ tend to be located after approximately one unit length downstream of the first obstacle. In the SF case, where the cavity is particularly short, this region of intense fluctuations is adjacent to the front face of the second obstacle. Both the first obstacle wake and the region in front of the second one exhibit high fluctuations in the WI case. In the IR case, the region of higher $k$ within the wake of the first obstacle does not reach the second one due to an even more extended cavity. However, the first obstacle's influence on the second is still very apparent. The most intense fluctuations around the second obstacle are generated in the separation region around the obstacle edges rather than in the wake. Note that this finding seems to contrast with the description of Oke [8], who found only negligible effects for the flow around the downstream obstacle for a similar cavity length.

The three diagonal components of the Reynolds-stress tensor have their maxima in different positions. The highest values of the streamwise normal stress are found in the upper region of the wake, in the high-shear flow immediately following the separation bubble on top of the first obstacle, and in the IR case in the turbulent region of separation on top of the second obstacle. As the distance between the obstacles increases, the streamwise normal Reynolds-stress values also increase in the region between the obstacle. This increment of $\overline{u^2}$ is probably connected to the interaction between low-momentum flow in the wake and high-momentum flow in the freestream. In fact, in the WI case, where the interaction between the layers of fluid is maximum within the cavity, the largest region of high values of $\overline{u^2}$ is observed. In addition, the values of $\overline{u^2}$ in the second obstacle wake are

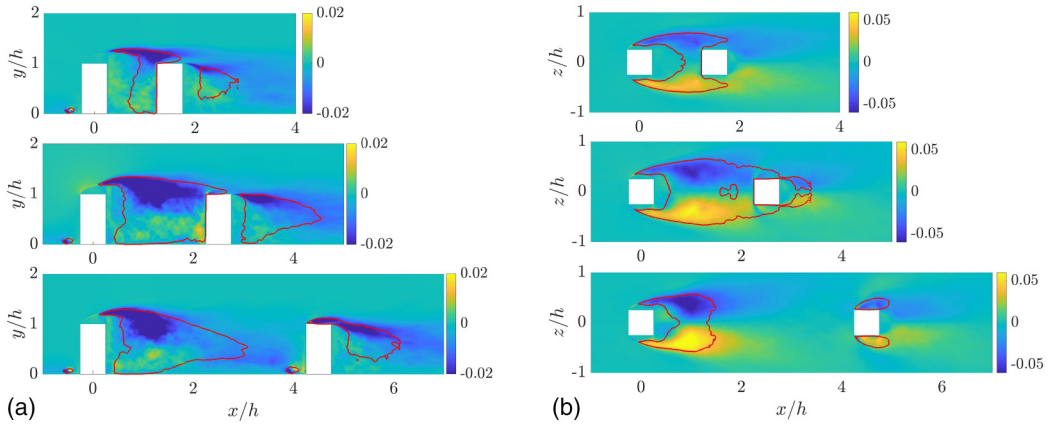


FIG. 9. Contour plots of the shear-Reynolds stresses (a) $\overline{uv}$ at $z/h = 0$ and (b) $\overline{uw}$ at $y/h = 0.25$. Note that a symmetric range of values is chosen for all figures, to help distinguish positive and negative values. The red contours denote regions of high turbulent kinetic energy $k$ reported as reference. In these regions, $k$ is higher than $1/3$ of its maximum in the domain. Shown from top to bottom are the SF, WI, and IR cases.

higher than those of the SF case. In the IR case, we observe that the region of high $\overline{u^2}$ between the two obstacles remains attached to the first one.

Regarding the vertical normal component of the Reynolds stresses (denoted by $\overline{v^2}$), in the SF regime, we find a region of high values attached to the front wall of the second obstacle. The strong fluctuations at the front wall of the second obstacle can be explained by interactions between the high-momentum fluid moving from the freestream, which descends into the cavity parallel to the front wall of the second obstacle, and the low-momentum fluid in the cavity. An increase in the distance between the obstacle, as we can see for the WI case, produces a new region of high $\overline{v^2}$ at the center of the cavity, as the mixing between flow in the cavity and flow outside the cavity becomes more pronounced. At the wake of the second obstacle, the region of high $\overline{v^2}$ is extended from that in the SF case. This extension is the result of the overall increase of turbulent fluctuations around the second obstacle, which is invested by flow with higher speed. In the IR case, intense vertical fluctuations are not present anymore in the region in front of the second obstacle.

The spanwise fluctuations $\overline{w^2}$ reflect the same trend as the other normal components of the Reynolds-stress tensor and further confirm the significant impact that the presence of the first obstacle still has on the second in the IR case.

The shear Reynolds stresses $\overline{uv}$ and $\overline{uw}$ are shown in Figs. 9(a) and 9(b), respectively. These quantities allow us to discuss the prevalent orientation of turbulent fluctuations. They both tend to be particularly intense in regions where the $\overline{u^2}$ also have higher values, i.e., in the upper region of the wakes and, in the IR case, in the turbulent region of separation on top of the second obstacle. The vertical shear Reynolds stress $\overline{uv}$ is negative in the regions where it is more intense, showing that turbulent fluctuations tend in general to drive momentum downward into the cavity. The extension of regions with different sign however varies between the three flow regimes. In the SF case, $\overline{uv}$ is positive in most of the cavity, including a relatively vast portion of space where the mean vertical velocity $\overline{V}$ is negative. In this case, mean advection contrasts with turbulent transport. In the WI case, which is the case with stronger mixing between the low-speed flow in the wake and the high-speed flow outside the wake, the region of negative and intense $\overline{uv}$ occupies the higher portion of the cavity. The region of positive $\overline{uv}$ underneath includes the location with the highest positive $\overline{uv}$ observed in the three cases, which is attached to the lower portion of the front face of the second obstacle. In this region again, relatively intense turbulent fluctuations have opposite orientation to the mean

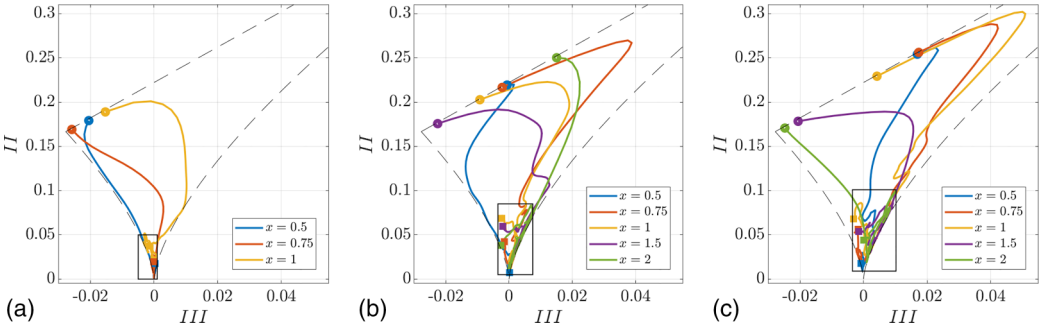


FIG. 10. Anisotropy-invariant maps for vertical profiles at the center plane and from $y/h = 0$ to 1 for cases (a) SF, (b) WI, and (c) IR. The circles and the squares on each line denote values at $y/h = 0$ and 1, respectively. Black rectangles enclose states at locations from the wall in the range $0 < y/h < 0.5$. Dashed black lines denote the theoretical limits to values of II and III.

advection. Finally, in the IR case, the region of intense negative $\overline{uv}$ is also limited to approximately two length units downstream of the first obstacle.

The horizontal shear Reynolds stress $\overline{uw}$ exhibits behavior similar to that of $\overline{uv}$, as turbulent fluctuation carries momentum towards the inner region of cavity. This term of the Reynolds stress however tends to be of higher values than $\overline{uv}$, because fluctuations in the spanwise direction are not limited by the presence of the ground as those in the vertical direction are. In particular, the pattern of $\overline{uw}$ on the left and the right of the obstacles tends to reproduce that of $\overline{uv}$ in the upper half of the cavities, in all cases.

We now consider the anisotropy-invariant maps (AIMs) to better describe how the structure of the turbulent flow within the cavity changes in the different cases. The anisotropy tensor, originally introduced by Lumley and Newman [66], is defined as

$$a_{ij} = \frac{1}{2}\frac{\overline{u_i u_j}}{k} - \frac{1}{3}\delta_{ij}, \tag{5}$$

and AIMs are constructed using its second and third invariants, i.e., $\mathrm{II} = a_{ij}a_{ji}$ and $\mathrm{III} = a_{ij}a_{in}a_{jn}$. The space of possible values of II and III is enclosed within boundaries determined by a set of limit cases: Three-dimensional (3D) isotropic turbulence, where energy is equally distributed in the three components, is ($\mathrm{II} = 0$, $\mathrm{III} = 0$); 2D isotropic turbulence is ($\mathrm{II} = 1/6$, $\mathrm{III} = -1/36$); and the limit of 1D turbulence is ($\mathrm{II} = 2/3$, $\mathrm{III} = 2/9$). The three paths between these limit cases are boundaries for allowed configurations and they represent axisymmetric contraction, between the 3D and 2D isotropic limits, $\mathrm{II} = 3/2(4/3\mathrm{III})^{2/3}$; axisymmetric expansion, between the 3D isotropic and 1D limits, $\mathrm{II} = 3/2(-4/3\mathrm{III})^{2/3}$; and the path between the 2D isotropic and 1D limit, $\mathrm{II} = 2/9 + 2\mathrm{III}$. In Fig. 10 we show the AIMs for a set of vertical profiles within the cavity for each case. For the SF case, we examine $x/h = 0.5$, 0.75, and 1 and for the WI and IR cases we also consider $x/h = 1.5$ and 2. The profiles are limited to the cavity region, i.e., $0 < y/h < 1$.

In all cases, the distributions of II and III move from the limit of 2D turbulence from the wall towards a state close to the limit of 3D isotropic turbulence far from the wall, as expected. This is particularly evident for the first profile ($x/h = 0.5$), in the proximity of the obstacle, where the mean velocity is relatively low at $y/h \approx 1$. In the SF case, along the first profile with a low turbulence intensity, we move from the 2D limit to the 3D limit almost following the axisymmetric contraction, with a predominance of flattened structures (so-called pancake-shaped turbulence). Moving along the second profile ($x = 0.5$), which is located at the middle of the cavity for this case, we transition from the 2D isotropic limit to the 3D isotopic state almost along the vertical line $\mathrm{III} = 0$. On the other hand, along the third profile ($x = 1$), where we observe stronger but still relatively low turbulent fluctuations, the AIM departs from the 2D limits. In the WI case,

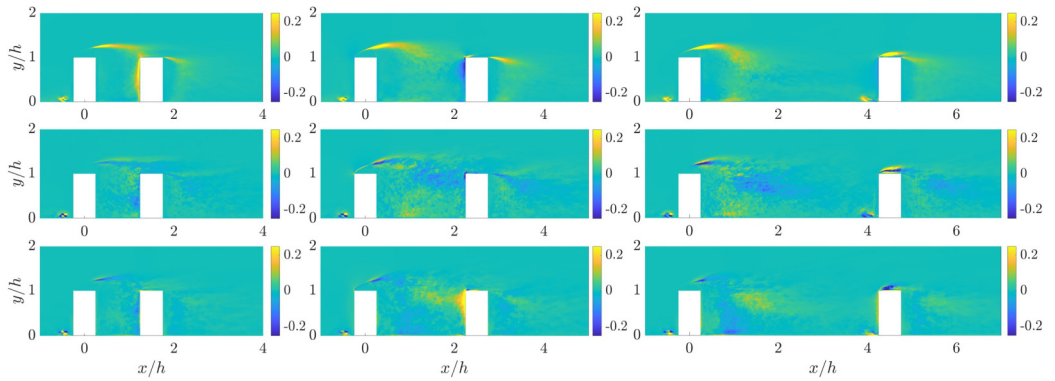


FIG. 11. Selected terms of the turbulent-kinetic-energy budget on the vertical plane $z/h = 0$. Shown from top to bottom are production, turbulent transport, and velocity-pressure-gradient correlation, denoted by $P_k$, $T_k$, and $\Pi_k$, respectively, and from left to right the SF, WI, and IR cases. Note that the same symmetric colormap is used, to highlight positive and negative values in all cases, even though it may not properly represent maxima and minima.

moving along the first profiles still means approaching the isotropic case from the 2D limit, as in the SF case. The profiles downstream however exhibit a different behavior. In correspondence with more intense turbulent fluctuations, turbulent structures depart more significantly from the 2D limit along the profile, and the state at $y = 1$ is farther from the 3D isotropic limit. A particularly evident distinction between the SF and WI cases is apparent along the profile closer to the second obstacle, which is at $x = 1$ for SF and $x = 2$ for WI. In the latter, in the proximity of the region with even more intense turbulent fluctuations, the AIM indicates a prevalence of elongated structures along the axisymmetric-expansion limit (so-called cigarlike turbulence). In the IR case, the profiles close to the first obstacle ($x = 0.5$, 0.75, and 1) exhibit an even more pronounced shift towards the 1D limit state than in the WI case. The profile $x = 1.5$ however is in good agreement with the same profile for the WI case, underling that structures in this region for the WI case are quite similar to those in the wake behind an isolated obstacle despite the proximity of the second obstacle. Finally, the profile $x = 2$ in the IR case, which is now behind the region with more pronounced fluctuations in the wake of the first obstacles, departs again from the 2D limit case at the wall with a trajectory closer to an axisymmetric contraction, but it also arrives at states with more elongated structures farther from the wall, with the same profile as in the WI case.

### C. Budget of the turbulent kinetic energy

To close the present discussion we will analyze terms of the TKE budget. We show production, turbulent transport, and velocity-pressure-gradient correlation in Figs. 11 and 12 for the vertical plane $z/h = 0$ and the horizontal plane $y/h = 0.25$, respectively. Each quantity is defined as described by Pope [67].

All terms of the TKE budget are virtually negligible in the freestream, away from the obstacles. On the other hand, most terms exhibit relatively high values in the horseshoe vortices. These vortices are always present in front of the first obstacle and the second one in the IR case. In the cavity and obstacle proximities, the three flow regimes differ significantly.

In the SF case, turbulent production, denoted by $P_k$, is particularly intense in three regions, i.e., immediately downstream of the separation region on top of the first obstacle, in front of the front face of the second obstacle, and downstream of the trailing edge of the second obstacle. In this case, $P_k$ is almost negligible within most of the cavity. In the WI case, a relatively large region with negative $P_k$ appears in front of the second obstacle and production occurs within the cavity. In the IR case, $P_k$ in the cavity is more intense just behind the first obstacle. Around the second

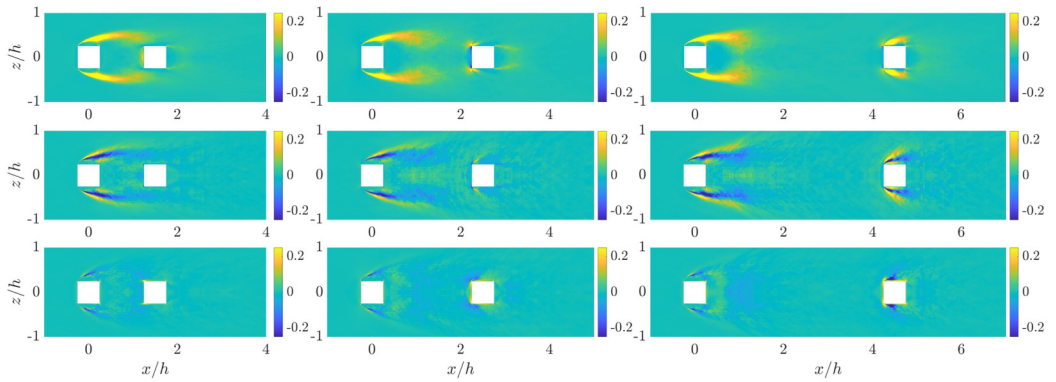


FIG. 12. Selected terms of the turbulent-kinetic-energy budget on the horizontal plane $y/h = 0.25$. Shown from top to bottom are production, turbulent transport, and velocity-pressure-gradient correlation, denoted by $P_k$, $T_k$, and $\Pi_k$, respectively, and from left to right the SF, WI, and IR cases. Note that the same symmetric colormap is used, to highlight positive and negative values in all cases, even though it may not properly represent maxima and minima.

obstacle, however, the most intense production occurs in the regions of separated flow adjacent to the faces. Interestingly, $P_k$ remains negative in front of the second obstacle in the IR case, even though it is much less intense in that region than in the WI case. The contours on the horizontal plane highlight the importance of high-shear regions on the sides faces of the first obstacles, which are also relatively similar for all cases.

Turbulent transport, denoted by $T_k$, tends to be negative in regions of very high turbulent fluctuations and positive in the adjacent regions where their intensity rapidly decreases. This fact is particularly apparent on the horizontal plane. In the SF case, $T_k$ is almost negligible in most of the cavity, where fluctuations are low, and it has negative values in front of the second obstacle, where we found the highest values of $\overline{v^2}$. In both the WI and IR cases, the turbulent transport is negative in the upper region of the wake and positive in the lower region, but in the IR case $T_k$ becomes negligible before the second obstacle.

The velocity-pressure-gradient correlation, denoted by $\Pi_k$, is negative in regions of very intense turbulent fluctuations, which is a trend similar to what is observed for the turbulent transport $T_k$. The change of sign of $\Pi_k$ in the region in front of the second obstacle is however particularly interesting. In the SF case, this term of the TKE budget is negative in that region. In the WI case, $\Pi_k$ becomes positive and reaches relatively high values there. In the IR case, $\Pi_k$ remains positive in front of the second obstacle, but its value decreases significantly. The qualitative behavior of $\Pi_k$ is then opposite to that of the production term, in this particular region of the domain.

We can discuss the TKE budgets in light of the anisotropy-invariant maps shown in the previous section. In the SF case, the profile at $x/h = 1$, which is in front of the second obstacle, roughly corresponds to the region of positive $P_k$, negative $T_k$, and negative $\Pi_k$, where the AIM indicates that turbulence is approaching the 3D isotropic limit along the asymmetric-contraction limit (pancake turbulence). In the WI case, downstream of the first obstacle, the distinction between the region close to the wall with positive $T_k$ and negative $\Pi_k$ and the region far from the wall with negative $T_k$ and positive $\Pi_k$ corresponds to the transition observed in the AIMs from states closer to the 2D limit to state closer to the 3D isotropic limit. The opposite signs of $T_k$ and $P_k$ in profiles $x/h = 2$ for the WI case and $x/h = 1$ for the SF case, which are the corresponding profiles at the front of the second obstacle, are linked to the fact that in the WI case those profiles exhibit states close the asymmetric-expansion limit (cigarlike turbulence).

Regarding the other terms of the TKE budget that are not shown here, they are viscous diffusion, pseudodissipation, and advection. Viscous diffusion is negligible, except for small near-wall regions

in all cases. Pseudodissipation is also relatively low if compared to the other terms of the budgets in most of the domain. Advection, denoted by $C_k$, reaches it highest positive values in the high-shear regions related to separation, similarly to what happens for the other terms already described. In the SF and WI cases, in the cavity, it has negative values in proximity to the front face of the second obstacle, where the mean vertical velocity is negative and carries turbulent kinetic energy downward. In the WI and IR cases, where a wake region is clearly distinguishable downstream of the first obstacle, $C_k$ exhibits positive values in the upper region of the wake and negative values in the lower region, which is qualitatively the opposite pattern to that of turbulent transport.

## IV. CONCLUSION

We have studied the results of highly resolved large-eddy simulations of the flow around two rectangular obstacles invested in a turbulent boundary layer. The Reynolds number based on the freestream velocity and obstacle height is $\mathrm{Re}_h = 10\,000$, whereas the incoming boundary layer reaches approximately $\mathrm{Re}_\tau = 170$ before the first obstacle. We considered three different configurations with various distances between the obstacles, corresponding to the three different flow regimes identified in the literature.

In the first regime, characterized by skimming flow, there is little penetration from the freestream into the cavity between the two obstacles, and the wake of the first one engulfs the second obstacle. In this case, the topology of the mean-velocity components is more similar to a cavity than a wake flow. In the second regime, characterized by wake interference, there are strong interactions between the freestream and the wake of the first obstacle. In the third regime, characterized by isolated roughness, the wake behind the first obstacle is not significantly affected by the presence of the second obstacle. In the first two cases, the reduced velocity of the incoming flow prevents separation from the edges of the second obstacle. In the IR case, separation around the second obstacle occurs, but the separation bubbles are smaller than those for the first obstacle.

The inflow conditions and the relatively high Reynolds number in our study, compared to previous numerical works with multiple obstacles, allowed us to discuss in detail the turbulent flow properties in the three regimes. This discussion included the distribution of turbulent fluctuations and terms of the turbulent-kinetic-energy budget, which were not considered in previous studies on similar geometries. Our analysis has identified three critical regions of the domain that are fundamentally affected by the increasing distance between the obstacles.

(i) The first region is immediately behind the first obstacle. This region is occupied by cavitylike flow in the SF case and wakelike flow in the WI and IR cases. The cavity flow exhibits lower turbulent fluctuations and TKE production to the wake flow.

(ii) The second region is adjacent to the second obstacle's front face. This region immediately reflects the more effective flow penetration from the freestream as the distances between obstacles increase. In the SF case, we have the most intense turbulent fluctuations and production of turbulent kinetic energy in this region. In the WI case, relatively intense turbulent fluctuations are still observed, but the production term of the TKE is negative, and turbulent kinetic energy is created with more complex mechanisms, as shown by the velocity-pressure-gradient correlation. In the IR case, turbulent fluctuations are less intense, and the classical horseshoe vortex is also present in front of the obstacle.

(iii) The last region, which changes more dramatically due to the increasing obstacle distance, immediately surrounds the second obstacle. In the SK and WI cases, there is no separation. In the IR case, there is mean separation and very intense turbulent fluctuations in the separation bubbles attached to the three faces.

There are also two regions of the domain where the increasing distance between obstacles has only mild repercussions. These are the surroundings of the first obstacle, as expected, and, perhaps more surprisingly, the wake of the second obstacle.

Important distinctions between the three regimes also appear in the anisotropy-invariant maps, which provide information about the structure of turbulence. In the SF case, there is a prevalence of

states close to the asymmetric-contraction limit within the cavity, including the region in front of the second obstacle with the more intense turbulent fluctuations and where TKE production is positive while the TKE turbulent transport and the velocity-pressure-gradient correlation are negative. On the other hand, at the corresponding location in the WI case, where turbulent fluctuations are also intense, there is a prevalence of states close to the asymmetric-expansion limit.

The results that we just summarized provide important indications for future works on similar geometries that will not employ high-fidelity numerical simulations. A similar distribution of turbulent fluctuations has to be obtained if particles or scalar dispersion are relevant in the conducted study, in particular if dispersion models are employed [68,69]. The anisotropy-invariant map that we showed also suggests a note of caution for the usage of turbulence models that employ a linear eddy viscosity hypothesis, as these models often fail to correctly predict anisotropy.

Nevertheless, our study has obvious limitations if the general context of urban flows is considered. The first limitation is the still very low Reynolds number compared with realistic length and velocity scales. It is reassuring to observe that our results are qualitatively similar to those in, e.g., the study by Zhao *et al.* [40] conducted at a Reynolds number 20 times lower than the present one. Our results also show the complexity of the turbulent flow in the three regimes, confirming that numerical studies at even higher Reynolds numbers may be required.

The second limitation is the simplicity of our configuration, which is evident in both inflow conditions and the obstacle geometry. The crucial phenomenon in the flow that originates from a boundary layer impacting a group of obstacles is the interaction of the wake created by leading obstacles with subsequent ones. In our idealized study case, this phenomenon was governed by the only geometrical parameter that we let vary, i.e., the obstacle distance. However, different obstacle alignments with the inflow velocity as well as different aspect ratios and relative sizes will lead to an even greater variety of flow regimes, indicating other possible directions for future investigations. A larger array of obstacles should also be considered to study the interaction between the wakes of obstacles farther downstream.

A further extension of the present study worth considering pertains to additional methodologies to characterize the different flow regimes. One approach is to examine coherent structures and link features of the instantaneous flow with the turbulence statistics that we considered here, following the work by Torres *et al.* [7], or causality analysis, as done by Martínez-Sánchez *et al.* [70]. A second approach is to determine how the three flow regimes differ in the dispersion of passive scalars and particles with inertia, which are both relevant in applications connected with pollution and pathogen contamination.

The data used to perform this study are available from the following repository: Urban flow statistics [71].

## ACKNOWLEDGMENTS

R.V. acknowledges financial support from the Göran Gustafsson Foundation. S.L.C. acknowledges Grant No. PID2020-114173RB-I00 funded by MCIN/AEI/10.13039/501100011033. M.A. acknowledges financial support from the Austrian Science Fund (FWF), Project No. I5180-N. This work was also supported by Grant No. RTI2018-102256-B-I00 of MINECO/FEDER. The meshes were generated using the SciDAX platform, which was developed by Parallel Works Inc. with support from the US Department of Energy, Office of Science, under Contract No. DE-SC0019695. The computations were enabled by resources provided by the Swedish National Infrastructure for Computing (SNIC) at the PDC Center for High Performance Computing, KTH Royal Institute of Technology, partially funded by the Swedish Research Council through Grant Agreement No. 2018-05973, where the funding provider is the Swedish Research Council.

[1] United Nations Environment Programme and United Nations Human Settlements Programme (UN-Habitat) (2021), Global Environment for Cities-GEO for Cities Towards Green and Just Cities. UNEP, Nairobi, available at https://unhabitat.org/sites/default/files/2021/11/geocities_updated.pdf.
[2] European Environment Agency, Air quality in Europe—2019 report, EEA Report No. 10/2019, 2019, available at https://www.eea.europa.eu/publications/air-quality-in-europe-2019.
[3] J. Lelieveld, K. Klingmüller, A. Pozzer, U. Pöschl, M. Fnais, A. Daiber, and T. Münzel, Cardiovascular disease burden from ambient air pollution in Europe reassessed using novel hazard ratio functions, Eur. Heart J. **40**, 1590 (2019).
[4] N. Isyumov, Studies of the pedestrian level wind environment at the boundary layer wind tunnel laboratory of the University of Western Ontario, J. Wind. Eng. Ind. Aerodyn. **3**, 187 (1978).
[5] R. Britter and J. Hunt, Velocity measurements and order of magnitude estimates of the flow between two buildings in a simulated atmospheric boundary layer, J. Wind. Eng. Ind. Aerodyn. **4**, 165 (1979).
[6] D. Zajic, H. J. S. Fernando, R. Calhoun, M. Princevac, M. J. Brown, and E. R. Pardyjak, Flow and turbulence in an urban canyon, J. Appl. Meteorol. Climatol. **50**, 203 (2011).
[7] P. Torres, S. Le Clainche, and R. Vinuesa, On the experimental, numerical, and data-driven methods to study urban flows, Energies **14**, 1310 (2021).
[8] T. Oke, Street design and urban canopy layer climate, Energy Build. **11**, 103 (1988).
[9] R. E. Britter and S. R. Hanna, Flow and dispersion in urban areas, Annu. Rev. Fluid Mech. **35**, 469 (2003).
[10] S. Di Sabatino, L. S. Leo, B. C. Hedquist, W. Carter, and H. J. S. Fernando, Eighth symposium on the urban environment, in *Proceedings of the 89th American Meteorological Society Annual Meeting, Phoenix, 2009* (American Meteorological Society, Washington, DC, 2009).
[11] A. U. Weerasuriya, K. T. Tse, X. Zhang, and S. W. Li, A wind tunnel study of effects of twisted wind flows on the pedestrian-level wind field in an urban environment, Build. Environ. **128**, 225 (2018).
[12] T. C. Corke, H. M. Nagib, and J. Tan-Atichat, Flow near a building model in a family of surface layers, J. Wind Eng. Ind. Aerodyn. **5**, 139 (1979).
[13] H. M. Nagib and T. C. Corke, Wind microclimate around buildings: Characteristics and control, J. Wind Eng. Ind. Aerodyn. **16**, 1 (1984).
[14] B. Monnier, B. Neiswander, and C. Wark, Stereoscopic particle image velocimetry measurements in an urban-type boundary layer: Insight into flow regimes and incidence angle effect, Bound.-Layer Meteorol. **135**, 243 (2010).
[15] B. Monnier, S. A. Goudarzi, R. Vinuesa, and C. Wark, Turbulent structure of a simplified urban fluid flow studied through stereoscopic particle image velocimetry, Bound.-Layer Meteorol. **166**, 239 (2018).
[16] H. J. S. Fernando, D. Zajic, S. Di Sabatino, R. Dimitrova, B. Hedquist, and A. Dallman, Flow, turbulence, and pollutant dispersion in urban atmospheres, Phys. Fluids **22**, 051301 (2010).
[17] G. Vita, Z. Shu, M. Jesson, A. Quinn, H. Hemida, M. Sterling, and C. Baker, On the assessment of pedestrian distress in urban winds, J. Wind. Eng. Ind. Aerodyn. **203**, 104200 (2020).
[18] M. Kanda, R. Moriwaki, and F. Kasamatsu, Large-eddy simulation of turbulent organized structures within and above explicitly resolved cube arrays, Bound.-Layer Meteorol. **112**, 343 (2004).
[19] Z. Xie and I. Castro, LES and RANS for turbulent flow over arrays of wall-mounted obstacles, Flow, Turbul. Combust. **76**, 291 (2006).
[20] Y. Tseng, C. Meneveau, and M. B. Parlange, Modeling flow around bluff bodies and predicting urban dispersion using large eddy simulation, Environ. Sci. Technol. **40**, 2653 (2006).
[21] O. Coceal, A. Dobre, T. G. Thomas, and S. E. Belcher, Structure of turbulent flow over regular arrays of cubical roughness, J. Fluid Mech. **589**, 375 (2007).
[22] Y. El-Okda, S. Ragab, and M. Hajj, Proceedings of the Fifth International Colloquium on Bluff Body Aerodynamics and Applications, Ottawa, 2004, edited by K. R. Cooper, G. L. Larose, and S. J. Zan [Large-eddy simulation of flow over a surface-mounted prism using a high-order finite-difference scheme, J. Wind. Eng. Ind. Aerodyn. **96**, 900 (2008)].
[23] E. Bou-Zeid, J. Overney, B. Rogers, and M. B. Parlange, The effects of building representation and clustering in large-eddy simulations of flows in urban canopies, Bound.-Layer Meteorol. **132**, 415 (2009).
[24] J. Santiago, A. Dejoan, A. Martilli, F. Martin, and A. Pinelli, Comparison between large-eddy simulation and Reynolds-averaged Navier-Stokes computations for the must field experiment. Part I: Study of the

flow for an incident wind directed perpendicularly to the front array of containers, Bound.-Layer Meteorol. **135**, 109 (2010).
[25] T. Kono, T. Tamura, and Y. Ashie, Numerical investigations of mean winds within canopies of regularly arrayed cubical buildings under neutral stability conditions, Bound.-Layer Meteorol. **134**, 131 (2010).
[26] M. Einian, D. J. Bergstrom, and D. Sumner, The effect of subgrid-scale model on prediction of flow around a surface-mounted finite square cylinder, J. Phys.: Conf. Ser. **318**, 042027 (2011).
[27] H. Nakayama, T. Takemi, and H. Nagai, LES analysis of the aerodynamic surface properties for turbulent flows over building arrays with various geometries, J. Appl. Meteorol. Climatol. **50**, 1692 (2011).
[28] H. Nakayama, T. Takemi, and H. Nagai, Large-eddy simulation of urban boundary-layer flows by generating turbulent inflows from mesoscale meteorological simulations, Atmos. Sci. Lett. **13**, 180 (2012).
[29] A. K. Saha, Unsteady flow past a finite square cylinder mounted on a wall at low Reynolds number, Comput. Fluids **88**, 599 (2013).
[30] M. Saeedi, P. P. LePoudre, and B.-C. Wang, Direct numerical simulation of turbulent wake behind a surface-mounted square cylinder, J. Fluid. Struct. **51**, 20 (2014).
[31] E. Joubert, T. Harms, and G. Venter, Computational simulation of the turbulent flow around a surface mounted rectangular prism, J. Wind. Eng. Ind. Aerodyn. **142**, 173 (2015).
[32] W.-C. Cheng and F. Porté-Agel, Adjustment of turbulent boundary-layer flow to idealized urban surfaces: A large-eddy simulation study, Bound.-Layer Meteorol. **155**, 249 (2015).
[33] R. Vinuesa, P. Schlatter, J. Malm, C. Mavriplis, and D. S. Henningson, Direct numerical simulation of the flow around a wall-mounted square cylinder under various inflow conditions, J. Turbul. **16**, 555 (2015).
[34] M. G. Giometto, A. Christen, C. Meneveau, J. Fang, M. Krafczyk, and M. B. Parlange, Spatial characteristics of roughness sublayer mean flow and turbulence over a realistic urban surface, Bound.-Layer Meteorol. **160**, 425 (2016).
[35] D. Zhang, L. Cheng, H. An, and M. Zhao, Direct numerical simulation of flow around a surface-mounted finite square cylinder at low Reynolds numbers, Phys. Fluids **29**, 045101 (2017).
[36] C. Diaz-Daniel, S. Laizet, and J. C. Vassilicos, Direct numerical simulations of a wall-attached cube immersed in laminar and turbulent boundary layers, Int. J. Heat Fluid Flow **68**, 269 (2017).
[37] I. Tolias, N. Koutsourakis, D. Hertwig, G. Efthimiou, A. Venetsanos, and J. Bartzis, Large eddy simulation study on the structure of turbulent flow in a complex city, J. Wind. Eng. Ind. Aerodyn. **177**, 101 (2018).
[38] P. Kumar and S. Tiwari, Wake transition for surface mounted rectangular cylinder due to incoming shear flow, Int. J. Heat Fluid Flow **85**, 108614 (2020).
[39] G. Tian, B. Conan, and I. Calmet, Turbulence-kinetic-energy budget in the urban-like boundary layer using large-eddy simulation, Bound.-Layer Meteorol. **178**, 201 (2021).
[40] M. Zhao, A.-A. Mamoon, and H. Wu, Numerical study of the flow past two wall-mounted finite-length square cylinders in tandem arrangement, Phys. Fluids **33**, 093603 (2021).
[41] J.-F. Sini, S. Anquetin, and P. G. Mestayer, Pollutant dispersion and thermal effects in urban street canyons, Atmos. Environ. **30**, 2659 (1996).
[42] J.-J. Baik and J.-J. Kim, A numerical study of flow and pollutant dispersion characteristics in urban street canyons, J. Appl. Meteorol. **38**, 1576 (1999).
[43] C.-H. Liu, Turbulent plane Couette flow and scalar transport at low Reynolds number, J. Heat Transf. **125**, 988 (2003).
[44] S. E. Belcher, Mixing and transport in urban areas, Philos. Trans. R. Soc. A **363**, 2947 (2005).
[45] P. Fischer, J. Lottes, and S. Kerkemeier, NEK5000: Open source spectral element CFD solver, 2008, available at http://nek5000.mcs.anl.gov.
[46] A. T. Patera, A spectral element method for fluid dynamics: Laminar flow in a channel expansion, J. Comput. Phys. **54**, 468 (1984).
[47] S. S. Varghese, S. H. Frankel, and P. F. Fischer, Direct numerical simulation of stenotic flows. Part 1. Steady flow, J. Fluid Mech. **582**, 253 (2007).
[48] A. Noorani, R. Vinuesa, L. Brandt, and P. Schlatter, Aspect ratio effect on particle transport in turbulent duct flows, Phys. Fluids **28**, 115103 (2016).

[49] R. Vinuesa, P. Schlatter, and H. M. Nagib, Secondary flow in turbulent ducts with increasing aspect ratio, Phys. Rev. Fluids **3**, 054606 (2018).
[50] L. I. Abreu, A. V. G. Cavalieri, P. Schlatter, R. Vinuesa, and D. S. Henningson, Spectral proper orthogonal decomposition and resolvent analysis of near-wall coherent structures in turbulent pipe flows, J. Fluid Mech. **900**, A11 (2020).
[51] A. Tanarro, R. Vinuesa, and P. Schlatter, Effect of adverse pressure gradients on turbulent wing boundary layers, J. Fluid Mech. **883**, A8 (2020).
[52] R. Vinuesa, L. Fick, P. Negi, O. Marin, E. Merzari, and P. Schlatter, Turbulence statistics in a spectral element code: A toolbox for high-fidelity simulations, Argonne National Laboratory Report No. ANL/MCS-TM-367 (OSTI, USA, 2017), https://doi.org/10.2172/1349052.
[53] M. P. Simens, J. Jimenez, S. Hoyas, and Y. Mizuno, A high-resolution code for turbulent boundary layers, J. Comput. Phys. **228**, 4218 (2009).
[54] S. Hoyas, M. Oberlack, F. Alcántara-Ávila, S. V. Kraheberger, and J. Laux, Wall turbulence at high friction Reynolds numbers, Phys. Rev. Fluids **7**, 014602 (2022).
[55] C. Canuto, M. Y. Hussaini, A. M. Quarteroni, and T. A. Zang, in *Spectral Methods in Fluid Dynamics*, edited by R. Glowinski, M. Holt, P. Hut, H. B. Keller, J. Killeen, S. A. Orszag, and V. V. Rusanov, Springer Series in Computational Physics (Springer, Berlin, 1988).
[56] F. Lluesma-Rodríguez, F. Álcantara Ávila, M. Pérez-Quiles, and S. Hoyas, A code for simulating heat transfer in turbulent channel flow, Mathematics **9**, 756 (2021).
[57] P. Schlatter, S. Stolz, and L. Kleiser, LES of transitional flows using the approximate deconvolution model, Int. J. Heat Fluid Flow **25**, 549 (2004).
[58] P. Negi, R. Vinuesa, A. Hanifi, P. Schlatter, and D. Henningson, Unsteady aerodynamic effects in small-amplitude pitch oscillations of an airfoil, Int. J. Heat Fluid Flow **71**, 378 (2018).
[59] S. Rezaeiravesh, R. Vinuesa, and P. Schlatter, An uncertainty-quantification framework for assessing accuracy, sensitivity, and robustness in computational fluid dynamics, J. Comput. Sci. **62**, 101688 (2022).
[60] J. Jeong and F. Hussain, On the identification of a vortex, J. Fluid Mech. **535**, 189 (1995).
[61] S. Dong, G. Karniadakis, and C. Chryssostomidis, A robust and accurate outflow boundary condition for incompressible flow simulations on severely-truncated unbounded domains, J. Comput. Phys. **261**, 83 (2014).
[62] P. Schlatter and R. Örlü, Turbulent boundary layers at moderate Reynolds numbers: Inflow length and tripping effects, J. Fluid Mech. **710**, 5 (2012).
[63] S. M. Hosseini, R. Vinuesa, P. Schlatter, A. Hanifi, and D. S. Henningson, Direct numerical simulation of the flow around a wing section at moderate Reynolds number, Int. J. Heat Fluid Flow **61**, 117 (2016).
[64] R. Vinuesa, A. Bobke, R. Örlü, and P. Schlatter, On determining characteristic length scales in pressure-gradient turbulent boundary layers, Phys. Fluids **28**, 055101 (2016).
[65] G. Eitel-Amor, R. Örlü, and P. Schlatter, Simulation and validation of a spatially evolving turbulent boundary layer up to $Re_\theta = 8300$, Int. J. Heat Fluid Flow **47**, 57 (2014).
[66] J. Lumley and G. Newman, The return to isotropy of homogeneous turbulence, J. Fluid Mech. **82**, 161 (1977).
[67] S. B. Pope, *Turbulent Flows* (Cambridge University Press, Cambridge, 2000).
[68] J.-P. Minier, E. Peirano, and S. Chibbaro, PDF model based on Langevin equation for polydispersed two-phase flows applied to a bluff-body gas-solid flow, Phys. Fluids **16**, 2419 (2004).
[69] M. Atzori, S. Chibbaro, C. Duwig, and L. Brandt, LES and RANS calculations of particle dispersion behind a wall-mounted cubic obstacle, Int. J. Multiph. Flow **151**, 104037 (2022).
[70] A. Martínez-Sánchez, E. López, S. Le Clainche, A. Lozano-Durán, A. Srivastava, and R. Vinuesa, Causality analysis of large-scale structures in the flow around a wall-mounted square cylinder, arXiv:2209.15356 [J. Fluid Mech. (to be published)].
[71] https://kth-my.sharepoint.com/:f:/g/personal/rvinuesa_ug_kth_se/EvQ_EyGeNIVHr3TZpzqC0hsBlWbopTScb8uH7Te053SxCQ?e=C5qZYu.

*Correction:* Error values in the eighth column of Table II have been fixed.